Vertical distributions of aerosol microphysical and optical properties based on aircraft measurements made over the Loess Plateau in China

Zhaoxin Cai [a,b,d], Zhanqing Li [h,**], Peiren Li [b], Junxia Li [c,*], Hongping Sun [b], Yiman Yang [e], Xin Gao [f], Gang Ren [b], Rongmin Ren [a], Jing Wei [g]

[a] State Key Laboratory of Remote Sensing Science, College of Global Change and Earth System Science, Beijing Normal University, Beijing, 100875, China
[b] Artificial Precipitation and Lightning Protection Technology Center, Meteorological Bureau of Shanxi Province, Taiyuan, Shanxi, 030032, China
[c] Key Laboratory for Cloud Physics of China Meteorological Administration, CMA Weather Modification Center, Chinese Academy of Meteorological Sciences, Beijing, 100081, China
[d] Meteorological Disasters Defense Technology Center, Meteorological Bureau of Shanxi Province, Taiyuan, Shanxi, 030032, China
[e] Fenghua District Meteorological Bureau, Ningbo, Zhejiang, 315500, China
[f] Service Center of Meteorological Bureau of Shanxi Province, Taiyuan, Shanxi, 030002, China
[g] Department of Chemical and Biochemical Engineering, Iowa Technology Institute, Center for Global and Regional Environmental Research, The University of Iowa, Iowa City, IA, USA
[h] Department of Atmospheric and Oceanic Science & Earth System Science Interdisciplinary Center (ESSIC), University of Maryland, 5825 University Research Court, Suite 4001, College Park, MD 20740-3823, USA

HIGHLIGHTS

- The major aircraft measurements were carried out and some new results were compared with previous campaigns.
- Vertical distributions of aerosol concentration, particle size, and optical properties were analyzed in the Loess Plateau.
- Long-distance transport of dust and local emission of BC were the main reasons for the absorption zone at high level.

ARTICLE INFO

ABSTRACT

Aerosol microphysical properties, scattering and absorption characteristics, and in particular, the vertical distributions of these parameters over the eastern Loess Plateau, were analyzed based on aircraft measurements made in 2020 during a summertime aircraft campaign in Shanxi, China. Data from six flights were analyzed. Statistical characteristics and vertical distributions of aerosol concentration, particle size, optical properties, including aerosol scattering coefficient (σ_{sp}), backscattering ratio (β_{sc}), Ångström exponent (α), single-scattering albedo (*SSA*), partially-integrated aerosol optical depth (*PAOD*), and black carbon concentration (BC_c), were obtained and discussed. Mean values of aerosol particle number concentration (N_a), particle volume concentration (V_a), mass concentration (M_a), surface concentration (S_a), and particle effective diameter (ED_a) were 854.92 cm^{-3}, 13.37 $\mu m^3\ cm^{-3}$, 20.06 $\mu g/m^3$, 170.08 $\mu m^3\ cm^{-3}$, and 0.47 μm, respectively. Mean values of BC_c, $\sigma_{sp\ (450,\ 525,\ 635\ nm)}$, $\beta_{sp\ (525\ nm)}$, $\alpha_{(635/450)}$, and SSA were 1791.66 ng m^{-3}, 82.37 Mm^{-1} at 450 nm, 102.57 Mm^{-1} at 525 nm, 126.60 Mm^{-1} at 635 nm, 0.23, 1.47, and 0.92, respectively. Compared with values obtained in 2013, N_a decreased by 60% and Ma decreased by 45%, but the scattering coefficients increased in different degrees. In the vertical direction, aerosol concentrations were higher at lower altitudes, decreasing with height. Vertical profiles of σ_{sp}, β_{sp}, $\alpha_{(635/450)}$, and BC_c measured during the six flights were examined. Two peaks in N_a were identified near the top of the boundary layer and between 2000 and 2200 m. Fine particles with ED_a smaller than 0.8 μm are dominant in the boundary layer and coarse aerosols existed aloft. Aerosol scattering properties and BCc in the lowest layer of the atmosphere contributed the most to the total aerosol radiative forcing. SSA values

were greater than 0.9 below 2500 m, with lower values at higher levels of the atmosphere. On lightly foggy days, SSA values were greater than 0.9, and aerosols played a cooling role in the atmosphere. On hazy days, lower-level SSA values were generally greater than 0.85, with aerosols likely having a warming effect on the atmosphere. 48-hour backward trajectories of air masses during the observation days showed that the majority of aerosol particles in the lower atmosphere originated from local or regional pollution emissions, contributing the most to the total aerosol loading and leading to high values of aerosol concentration and radiative forcing.

1. Introduction

Atmospheric aerosols refer to solid and liquid particles suspended in the atmosphere. Atmospheric aerosols directly affect Earth's radiative budget by scattering and absorbing solar and thermal radiation (Haywood and Shine, 1997) further affecting the environment and climate (Horvath, 1995; Li et al., 2016, 2019). The aerosol particle size distribution, chemical composition, and mixing state mainly determine aerosol optical properties (Jennings et al., 1978). Most organic and inorganic aerosol particles scatter sunlight (Bohren et al., 1998), while black carbon, brown carbon, and dust particles absorb sunlight (Bond et al., 2013). Objective and accurate measurements of aerosol optical properties are thus important for calculating the radiative forcing and evaluating the climate effect (CHARLSON et al., 1992).

Over the past years, observational studies focusing on near-surface physical, chemical, and optical properties of aerosols have been carried out in different regions of China (Li et al., 2016, 2017a,b), including the Tibet Plateau (Bai et al., 2000), the northwest region (Yan, 2007), the North China Plain (Ke and Tang, 2007; Yan et al., 2008; X. Zhao, 2011), the Yangtze River Delta region (Zhuang et al., 2015), the Pearl River Delta region (Wu et al., 2009), and some high-altitude regions, e. g., Huangshan Mountains (Yuan et al., 2016, 2019) and Mount Taishan (Yamaji et al., 2010). The effect of aerosols on radiation is also closely related to the aerosol vertical distribution because aerosol properties are complex, changing rapidly in the vertical direction. Large uncertainties still remain in studying aerosol particles, especially the vertical distributions of aerosols in the lower troposphere and the stratosphere (Stettler and von Hoyningen-Huene, 1996; Deshler, 2008). There is thus still an urgent need to better understand the vertical distributions of aerosol properties. Satellite remote sensing provides global scale observations to portray the spatial and temporal variations of various atmospheric parameters including aerosols. Johnson et al. (2009) utilized aircraft, satellite and ground-based remote sensing data to analyze the vertical distributions of dust and biomass-burning aerosols. Using the Ozone Monitoring Instrument (OMI) data, Kang et al. (2017) found that the absorbing aerosols over East Asia have increased over time. The vertical variations of haze microphysical and optical properties in Shanghai were analyzed based on satellite observation by Geng et al. (2011) and Chen et al. (2012) respectively. Shen et al. (2020) comprehensively utilized ground-based remote sensing and Cloud-Aerosol Lidar and Infrared Pathfinder Satellite Observations (CALIPSO) data to analyze the optical characteristics and vertical distribution characteristics of aerosols over Nanjing. Song et al. (2020) found the dust aerosols were more efficiently transported to the adjacent ocean and other non-desert regions such as the Central Atlantic, North China Plain, and Arabian Sea based on CALIPSO. And at present, in situ measurements of aerosol vertical distributions are also made from towers, tethered balloons, unmanned aerial vehicles (UAVs), and aircraft. However, towers, tethered balloons, and UAVs have disadvantages, such as height restrictions (Y. Sun et al., 2010; Ferrero et al., 2014; Höpner et al., 2016). Aircraft have the main advantage of obtaining detailed information about aerosol properties at different levels in the atmosphere. However, aircraft campaigns are of short duration, covering limited geographic areas. Nevertheless, aircraft are considered to be one of the most suitable platforms from which to observe the vertical distribution of aerosols and to measure their physical and optical properties (Bodhaine et al., 1991; Hänel, 1998; Welton et al., 2002; Anderson et al., 2003b; Han et al.,

2003; Raut and Chazette, 2008; Li et al., 2015a, 2015b, 2019a,b; Yang et al., 2020). Aircraft-based field campaigns measuring the physical, chemical, and optical properties of aerosols have been carried out around the world, e.g., the Smoke, Clouds, and Radiation-Brazil experiment (Kaufman et al., 1998), the Tropospheric Aerosol Radiative Forcing Observational Experiment (Russell et al., 1999), the 2nd Aerosol Characterization Experiment (Raes et al., 2000), and the Indian Ocean Experiment (Ramanathan et al., 2001), providing a picture of the vertical distributions of aerosol optical properties in different parts of the world.

Existing aircraft measurements have shown that aerosol spatial distributions, particle sizes, and shapes, as well as particle chemical compositions, are strongly affected by their sources and the aging process, with aerosol properties varying greatly in different regions, at different times, and under different background weather conditions. Aerosol optical properties in Asia differ greatly from those in Europe and North America (Hu et al., 2020). Some aircraft field campaigns have taken place in China, e.g., in Beijing (Liu et al., 2009), Hebei (Wang et al., 2018), and Shanxi (Li et al., 2015a, 2017a,b). However, these experiments mainly focused on the aerosol scattering coefficient (σ_{sp}).

The Loess Plateau covers most of Shanxi Province in northern China, with the North China Plain to the east. The average surface altitude above sea level (ASL) of the entire province is 1000 m. As one of the most important chemical industrial bases in China, experiencing rapid economic growth, the mixture of heavy air pollution from industrial activities results in complex local aerosol physical and optical properties (Zeng et al., 2019; Zhang et al., 2012). In recent years, to save energy and reduce emissions in China, the emissions of major air pollutants have decreased and the air quality has substantially improved (B. Zheng et al., 2018), the relative change rates of Shanxi's anthropogenic emissions during 2010–2017 are estimated as follows: -42.3% for TSP, -34.8% for $PM_{2.5}$, -36.6% for PM_{10}, -25.2% for CO, -48.4% for SO_2, -21.5% for NO_X, -43.2% for BC, -45.6% for OC, $+10.5\%$ for NH_3 and -0.4% for VOC (data from http://meicmodel.org). The physical, chemical, and optical properties of aerosols have changed greatly in this region. In order to examine if such drastic changes in the emissions of aerosol precursor gases have any discernible impact on aerosol and cloud condensation nuclei, an airborne field campaign was conducted from 10 June to August 10, 2020 in Shanxi Province as a key part of the Joint Airborne and Ground-based Aerosol-Convective Cloud Interactions Observation Experiment. Note that a previous experiment was conducted in 2013 in the same region and season (Li et al., 2015a, 2015b, 2015b). Data from four flights were used to analyze the aerosol optical properties at three observation sites in Taiyuan (TY), Wenshui (WS, about 80 km southwest of TY), and Xinzhou (XZ, 80 km north of TY), respectively. The observational data were analyzed, although their representativeness was poor due to very small data samples. More importantly, the influence of aircraft exhaust emissions during hover flight was not taken into account, leading to a somewhat erroneous result. Taking these shortcomings into consideration, we have improved the flight plan. The flight was only conducted in XZ area. The radius of flight circle was less than 5 km, and the statistical results were more representative. In addition, only the first vertical profile observed each time was selected in the analysis to minimize the impact of aircraft exhaust on the environment. The results of the two observation experiments will also be compared and analyzed in this study.

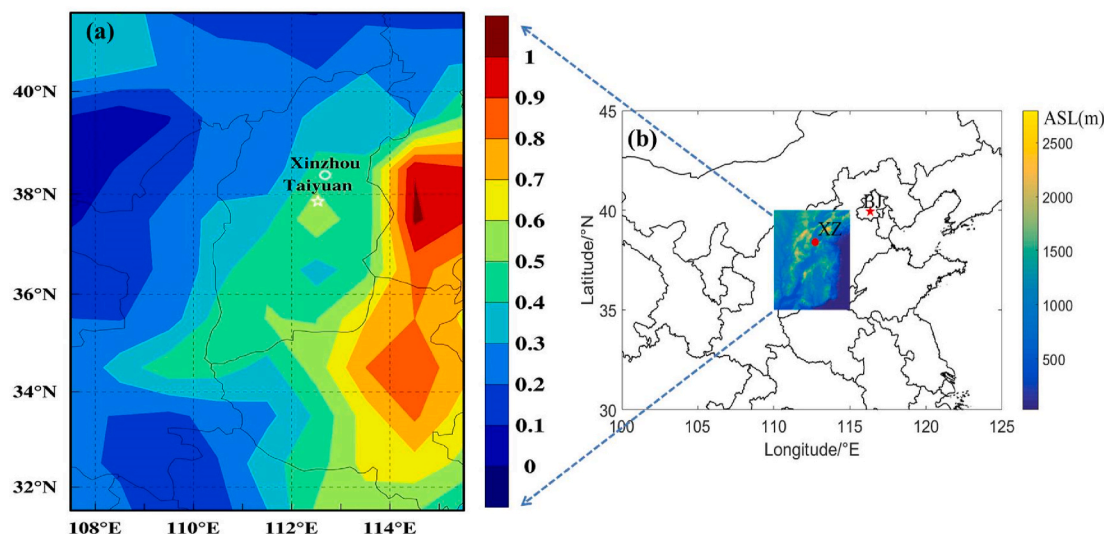In this study, aerosol microphysical properties and scattering/

Fig. 1. Map of Shanxi Province in North China. (a) Locations of the observation site (Xinzhou, white circle) and Taiyuan City (white star). The colored background shows the mean aerosol optical depth from 10 June to August 10, 2020 obtained from Moderate Resolution Imaging Spectroradiometer data. (b) Map of the observation area in North China, showing the locations of the Xinzhou (XZ) site (red dot) and Beijing City (BJ, red star). The color bar represents the altitude above sea level (ASL). (For interpretation of the references to color in this figure legend, the reader is referred to the Web version of this article.)

absorption characteristics, especially vertical distributions of these parameters over the eastern Loess Plateau, were analyzed based on aircraft measurements. This provides the basis for calculating and evaluating the direct radiative effect of aerosols in the middle and lower troposphere. The paper is organized as follows. Section 2 describes the observation area and provides details about the aircraft campaign and datasets. Section 3 presents detailed analyses and discussion of the measured results. Section 4 show the simulation of 48-h backward trajectories of air masses and comparison with a previous air campaign. Section 5 gives conclusions.

2. Description of the field campaign

2.1. Location

Field measurements were made from 10 June to August 10, 2020 at the meteorological station (112°41′41″E, 38°23′37″N, 870 m ASL) in Xinzhou (XZ). This site is located 60 km northeast of Taiyuan City (TY, the capital of Shanxi Province). The observatory is surrounded by agricultural land, with no high buildings in the immediate surroundings. Fig. 1 shows the locations of TY City and XZ, as well as the distribution of mean aerosol optical depth (AOD) over Shanxi Province during the field campaign. AODs over Shanxi Province decreased gradually from southeast to northwest. The AOD over the XZ station was about 0.4–0.5 on average, and over TY City, about 0.5–0.6 on average. The relatively low values of observed AOD at XZ suggest that this site were slightly polluted.

2.2. Instruments

A Y-12 turboprop airplane was used as the aerosol observation platform. The typical speed of the aircraft was about 60–70 m s^{-1}, and the rate of ascent or descent of the aircraft was about 2–6 m s^{-1}. The aircraft is not an airtight cabin, and the temperature difference between the inside cabin and the outside environment is very small. It was equipped with multiple instruments measuring different aerosol properties. Each instrument was calibrated and tested rigorously during a ground-based campaign prior to the airborne campaign, ensuring that the instruments were functioning properly.

An air sampling inlet device made of stainless steel was mounted on top of the airplane fuselage, with a stents height of about 10 cm. The air

inlet was connected to the sampling equipment inside the aircraft through straight stainless steel tubes and non-adsorption rubber hose. The collection efficiency for aerosol particles in the size range of 0.01–5.0 μm was 95%, and the collection efficiency of aerosol particles with size larger than 5.0 μm was about 50%. Without using an air pump, the air inlet flow was about 15 L/min, which can be used in the range of 200–300 km/h flight speed. In order to ensure the air sampling efficiency, a 50 L/min suction pump was installed in the aircraft cabin to ensure sufficient sampling airflow for the instrument, and to minimize particle losses in inlet system.

The inlet was connected to the instruments in as direct a way as possible to avoid turns or corners. Ambient air was pumped into the aircraft cabin from the sample inlet, entering into each instrument after drying. The relative humidity (RH) of sampled air after drying was less than 40%.

A three-wavelength (450 nm, 525 nm, 635 nm) integrating nephelometer (Aurora-3000, Ecotech, Australia) was used to measure σ_{sp}. This instrument can measure particle optical scattering in the ambient atmosphere continuously in real time, obtaining the total σ_{sp} and the backscattering coefficient (σ_{bsp}) (90–170°) with a sampling interval of 1 min.

A five-wavelength (880 nm, 625 nm, 528 nm, 470 nm, 375 nm) black carbon (BC) analyzer (MA-200, Aethlabs, USA) was used to measure BC mass concentrations and light absorption with a sampling interval of 150 mL min^{-1} flow rate and 1 s time resolution. Measurement at 880 nm is interpreted as the concentration of Black Carbon (BC). Measurement at 375 nm is interpreted as Ultraviolet Particulate Matter (UVPM) indicative of organic sources such as wood smoke, tobacco, and biomass burning. The MA-200 also features the loading compensation method, which in real-time measures and adjusts for different optical properties of particles of varying age and composition (Drinovec et al., 2015; Wang et al., 2020). In this experiment, a valve for restricting flow was installed in front of the MA-200, and a small pump was installed inside the MA-200 to ensure a smooth air inlet.

A passive cavity aerosol spectrometer probe (PCASP-100X, DMT, USA) was used to observe aerosol particles with diameters ranging from 0.1 to 3.0 μm in 30 bins of variable size with a frequency of 1 Hz. From this information, aerosol concentrations and particle sizes were derived. The PCASP was calibrated using polystyrene latex spheres before measurements took place.

A meteorological package called the Aircraft Integrated

Table 1
Flight summary [date: yy-mm-dd, time: hh:mm (CST), height: m (ASL)].

Date	Total flight time	Flight period over the observatory				
		Time	T (°C)	RH (%)	Vertical height (m)	Weather condition
2020-7-15	16:50–18:53	17:40–18:13	0.67–24.34	44.08–93.74	1193–5018	Light fog
2020-7-16	11:46–16:20	14:00–15:26	−0.6–26.6	45–81	1121–5373	Haze
2020-7-24	13:55–16:58	14:44–16:03	8.09–25.59	22.78–77.84	1191–3832	Clear
2020-7-27	16:28–19:32	18:08–18:34	5.09–25.24	65.39–96.26	1147–3670	Light fog
2020-7-30	14:45–18:55	16:51–18:11	−2.24–27.99	32.39–90.75	1185–4796	Haze
2020-8-3	15:06–17:50	15:47–17:18	6.98–28.36	25.14–47.98	1141–3787	Clear

Meteorological Measurement System (AIMMS-20, Aventech Research Inc., Canada) measured meteorological parameters including ambient temperature (T), RH, and location (e.g., longitude, latitude, and altitude) at a frequency of 1 Hz. Temperatures measured by the AIMMS-20 range from −20 °C to 40 °C with a detection accuracy of 0.3 °C, and the RH detection accuracy is 2.0% with a resolution of 0.1%.

Before each flight, all instruments were calibrated, and the air tightness of the gas path and each instrument was checked with a hand-held manometer.

2.3. Datasets

The main parameters studied in this paper are as follows. The PCASP provided aerosol particle number concentrations (N_a, cm^{-3}). The aerosol particle effective diameter (ED_a, μm), particle volume concentration (V_a, μm^3 cm^{-3}), mass concentration (M_a, μg m^{-3}), and surface concentration (S_a, μm^2 cm^{-3}) were derived from the particle number spectrum. Note that data from the PCASP in the first bin (0.09–0.1 μm) are inaccurate due to the detection limit of the instrument, so they were eliminated from the analysis (Li et al., 2015a, 2015b, 2019a,b; Sun et al., 2016).

The scattering coefficient ($\sigma_{sp}(\lambda)_{450,\ 525,\ 635\ nm}$) and backscattering coefficient ($\sigma_{bsp}(\lambda)_{450,\ 525,\ 635\ nm}$) (Mm^{-1}) were obtained directly from the Aurora-3000 nephelometer, and according to Wu et al. (2012), revised the truncation error. The backscattering ratio (β_{sc}) and the ratio of aerosol backscatter coefficient to total scattering coefficient (σ_{bsc}/σ_{sc}) are other important parameters examined here, used to determine the fine-particle content of the total aerosol loading.
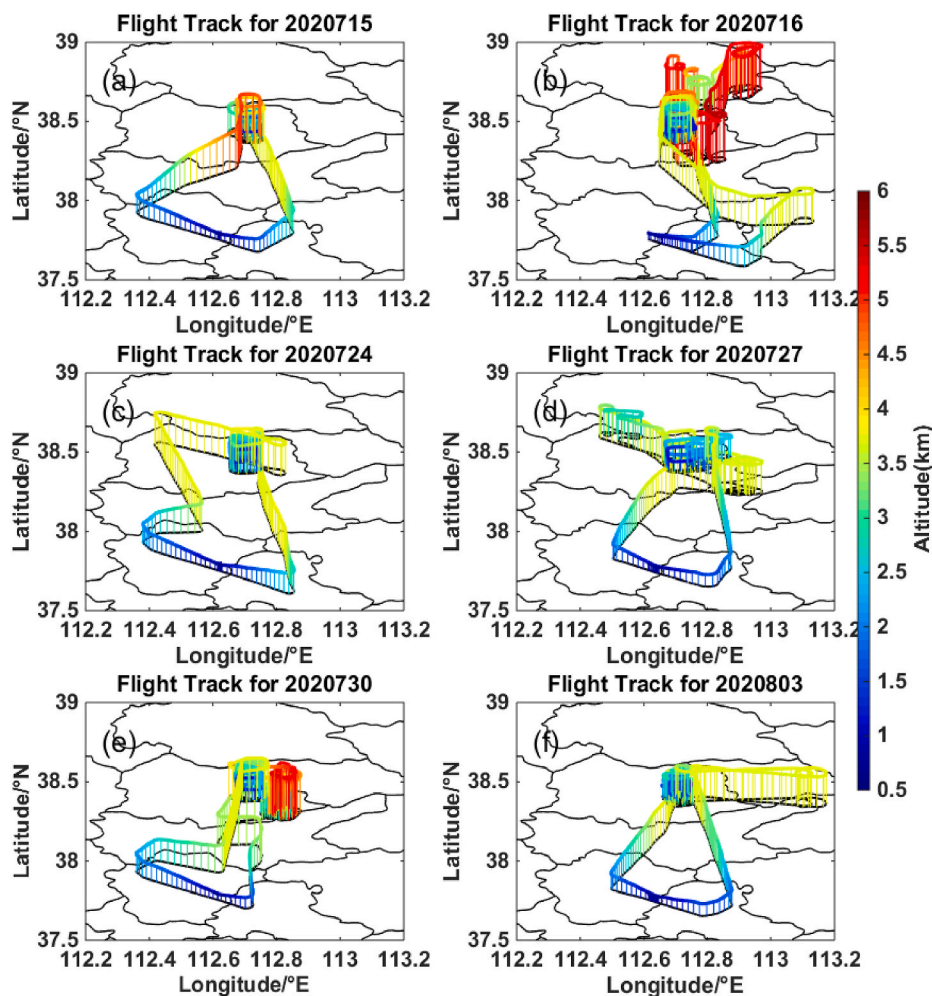

Fig. 2. Flight tracks made on (a) 15 July, (b) 16 July, (c) 24 July, (d) 27 July, (e) 30 July, and (f) August 3, 2020. The color bar shows the height above sea level (ASL) in km. Note that the aircraft circled the XZ site at different heights. (For interpretation of the references to color in this figure legend, the reader is referred to the Web version of this article.)
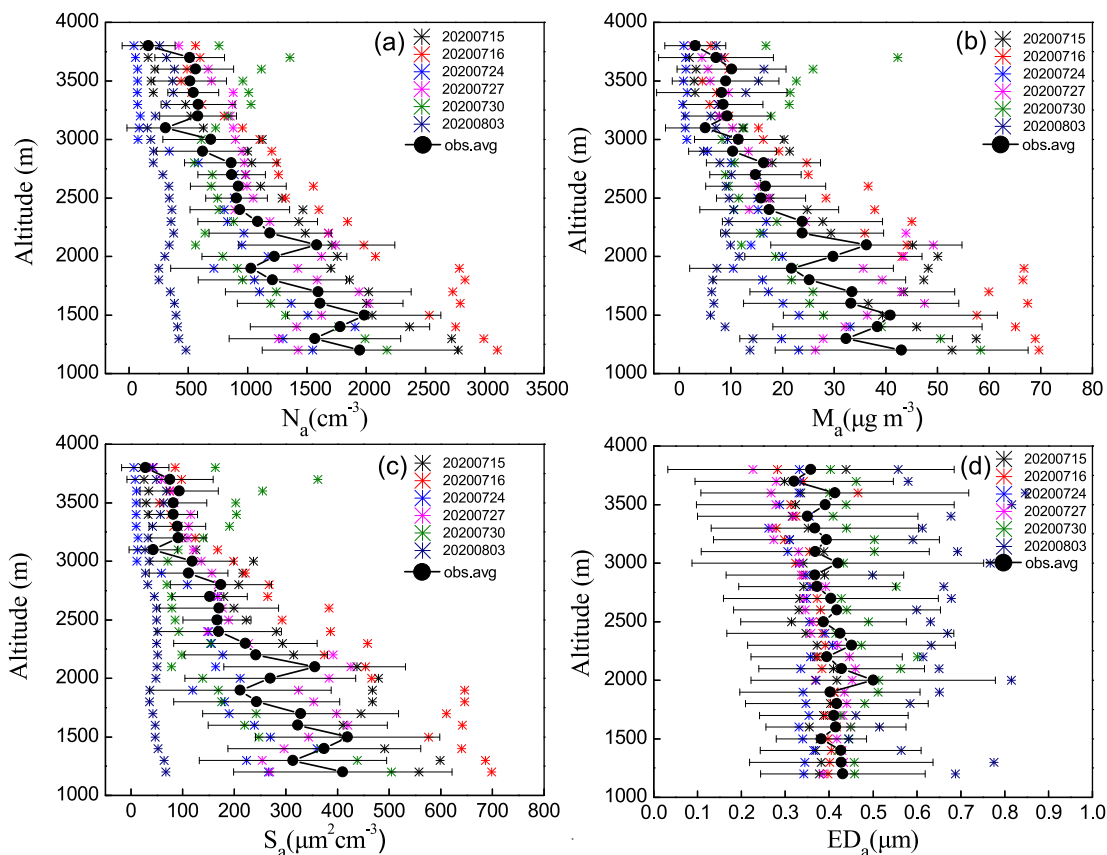
Fig. 3. Vertical profiles of mean (a) aerosol particle number concentrations (N_a), (b) mass concentration (M_a), (c) surface concentration (S_a) and (d) aerosol particle effective diameter (ED_a) from all flights. Colored asterisks represent observations made on different days. Horizontal black lines show the range of values (mean and standard deviation values) observed at each altitude level (ASL).

The Ångström exponent (α), which characterizes the wavelength dependence of σ_{sp}, was obtained, providing information on the size distribution of particles, i.e., the relative amount of fine and coarse particles, which differs according to the aerosol type (Seinfeld and Pandis, 1998). The BC mass concentration (BC_c, ng m^{-3}) was obtained from the MA-200 instrument, and we use the Optimized Noise-reduction Averaging (ONA) algorithm (Hagler et al., 2011) for signal noise reduction. After the ONA treatment, the data were further corrected for the loading effect following the algorithm of Virkkula et al. (2007).

The single scattering albedo (SSA), the ratio of scattering coefficient to total extinction coefficient (σ_{ext}), is calculated based on Eq. (1).

$$SSA(\lambda) = \frac{\sigma_{sp}(\lambda)}{\sigma_{ext}(\lambda)} = \frac{\sigma_{sp}(\lambda)}{\sigma_{sp}(\lambda) + b_{abs}(\lambda)} \tag{1}$$

Equation (1) was used to calculate the particle absorption coefficient (b_{abs}) ($\lambda = 375, 470, 528, 625, 880$ nm) (Mm^{-1}):

$$b_{abs}(\lambda) = BCc(\lambda) \times 0.001 \times \sigma(\lambda) \tag{2}$$

where $\sigma(\lambda)$ (m^2 g^{-1}) is the mass absorption cross-section at the 5 different wavelengths. The values of $\sigma(\lambda)$ are 24.069, 19.070, 17.028, 14.091, and 10.120 at 375, 470, 528, 625, and 880 nm, respectively (Wang et al., 2020).

2.4. Flights

Six flights were conducted during the 2020 field campaign, i.e., on 15, 16, 24, 27, 30 July, and 3 August. Regarding atmospheric conditions at the observation station, there was light fog on 15 and 27 July, haze on 16 and 30 July, and clear skies on 24 July and 3 August. The aircraft was based at Taiyuan Wusu International Airport and flew from there to XZ,

then carried out vertical flight observation over XZ station with a flight radius of 5 km, focusing on the vertical distribution of aerosols over the station. Table 1 provides flight details, and Fig. 2 shows the flight tracks. Note that all times are in China Standard Time (CST).

3. Observation results

3.1. Vertical profiles of Na and ED

Fig. 3 shows the mean vertical profiles of aerosol number concentration (Fig. 3a), mass concentration (Fig. 3b), surface concentration (Fig. 3c), and particle effective diameter (Fig. 3d) from the six flights, averaged over every 100 m. Vertical profiles of aerosols differed depending on the weather conditions. On 24 July and 3 August, the sky was clear, and N_a was relatively small. Haze occurred on 16 and 30 July, leading to relatively larger values of N_a, especially on 16 July. From the average profile of N_a (Fig. 3a), values of N_a fluctuated from near the ground (1200 m) to 1500 m, where the first peak was reached. Large amounts of aerosol particles were constrained to the lower layer of the atmosphere (below 1500 m), likely attributed to the effects of the atmospheric boundary layer. The six flights were all carried out in the afternoon. The average boundary-layer height within the observation period was 1528 ± 193 m, according to ground lidar observations made during the same time range. The atmospheric boundary layer often hinders the vertical transmission and dispersion of aerosols and other pollutants, so large amounts of aerosol particles can accumulate within the boundary layer. The second peak of N_a was located between 2000 m and 2200 m, decreasing with height. The vertical profiles of M_a and S_a were similar to that of N_a. Mean values of N_a, M_a, and S_a generally decreased gradually with height.
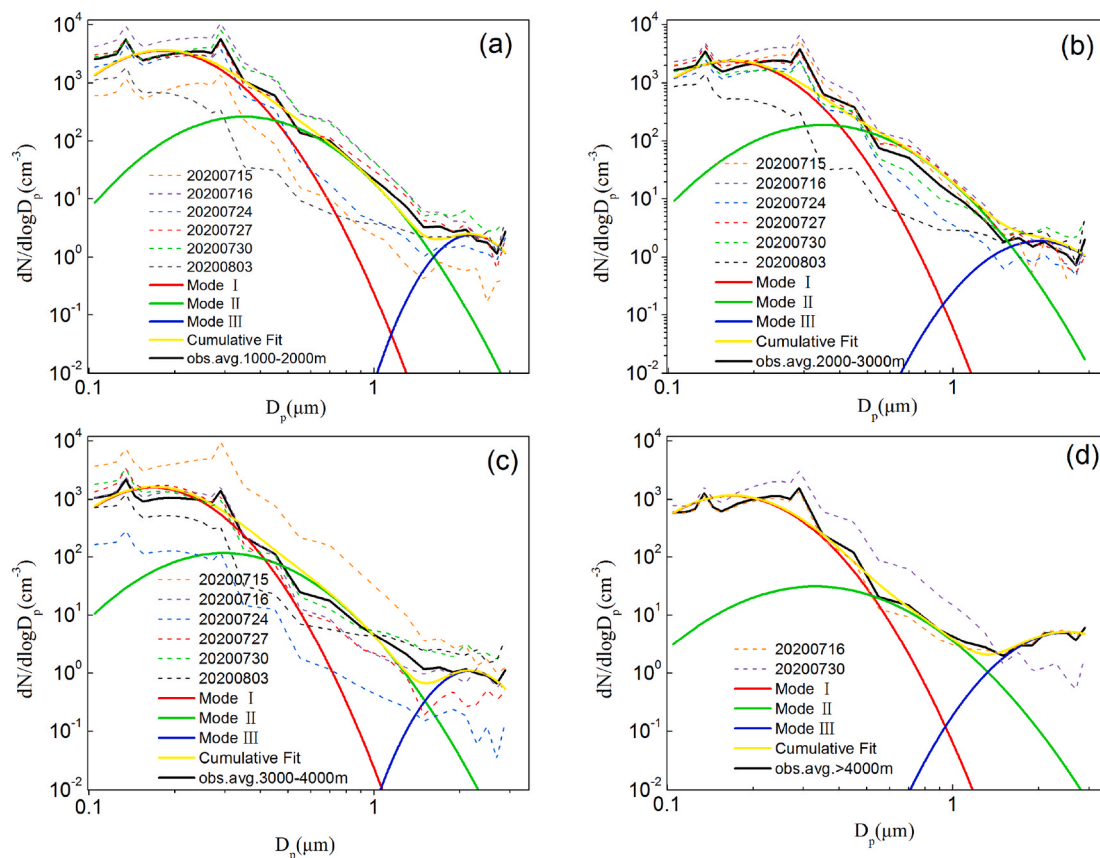
Fig. 4. Mean aerosol particle size distributions of aerosol particles at (a) 1000–2000 m, (b) 2000–3000 m, (c) 3000–4000 m, and (d) above 4000 m from six flights during the field campaign. The dotted lines of different colors represent the size distributions of aerosol particles on each day, and the thick black lines denote the mean states of the total aerosol particle size distribution. The solid yellow lines are the fittings of particle spectral distributions, and the red (Mode I), green (Mode II), and blue (Mode III) solid lines represent the lognormal fits of the three aerosol mode size distributions, respectively. (For interpretation of the references to color in this figure legend, the reader is referred to the Web version of this article.)

The mean ED_a vertical profile (Fig. 3d) showed no clear trend with altitude, other than a slight increase with height. In general, ED_a was less than 0.8 μm. Two peaks in ED_a were identified: one between 1900 and 2300 m and the other above 3500 m. The combination of information from vertical profiles of aerosol concentration and ED_a can help determine the source of the aerosol particles. The majority of aerosols below 2100 m were fine-mode particles with ED_a less than 0.5 μm, suggesting that these particles may have originated from local or regional pollution emissions. Relatively larger particles distributed at higher altitudes suggest that these particles were transported to the XZ region from desert areas afar.

Among the six flights, no precipitation occurred for several consecutive days before the flight observation on August 3, and the meteorological background condition was different from the others. In addition, according to the results of backward trajectory (Section 4.1), the aerosols observed on August 3 were mainly dust transported from Mongolia and Inner Mongolia, with a few local aerosol emission. So, the corresponding physical characteristic parameters of aerosol collected on 20200803 deviated significantly from the others.

3.2. Number size distribution of aerosol particles

The distribution of N_a with particle size, called as the particle size spectral distribution, is an important parameter used to describe the features of aerosol particle distributions. The average aerosol particle number size distributions from the all flights in this study and the mean state of the aerosol particle size distribution are shown as Fig. 4. Compared with the results obtained in 2013 (Li et al., 2015b), the N_a in the range of 0.1–0.5 μm and 0.8–3 μm decreased by 32.4% and 72.1%, respectively. However, the N_a in the range of 0.5–0.8 μm increased by 15.8%. A multi-lognormal distribution function, as in Equation (3), was used to fit the measured aerosol number size distributions (Sun et al., 2013; Li et al., 2015b; Hao et al., 2017; Yang et al., 2020):

$$\frac{dN(D)}{d\log(D_P)} = \sum_{i=1}^{n} \frac{N_i}{\sqrt{2\pi}\log(\sigma_{g,i})} \exp\left[-\frac{(\log(D_p) - \log(D_{g,i}))^2}{2(\log\sigma_{g,i})^2}\right] \quad (3)$$

where n is the number of modes per size distribution for the best fit, D_p is the peak aerosol diameter, N_i is the aerosol number in mode i, $D_{g,i}$ is the

Table 2
Parameters characterizing the number size distributions of the three aerosol modes at different altitudes.

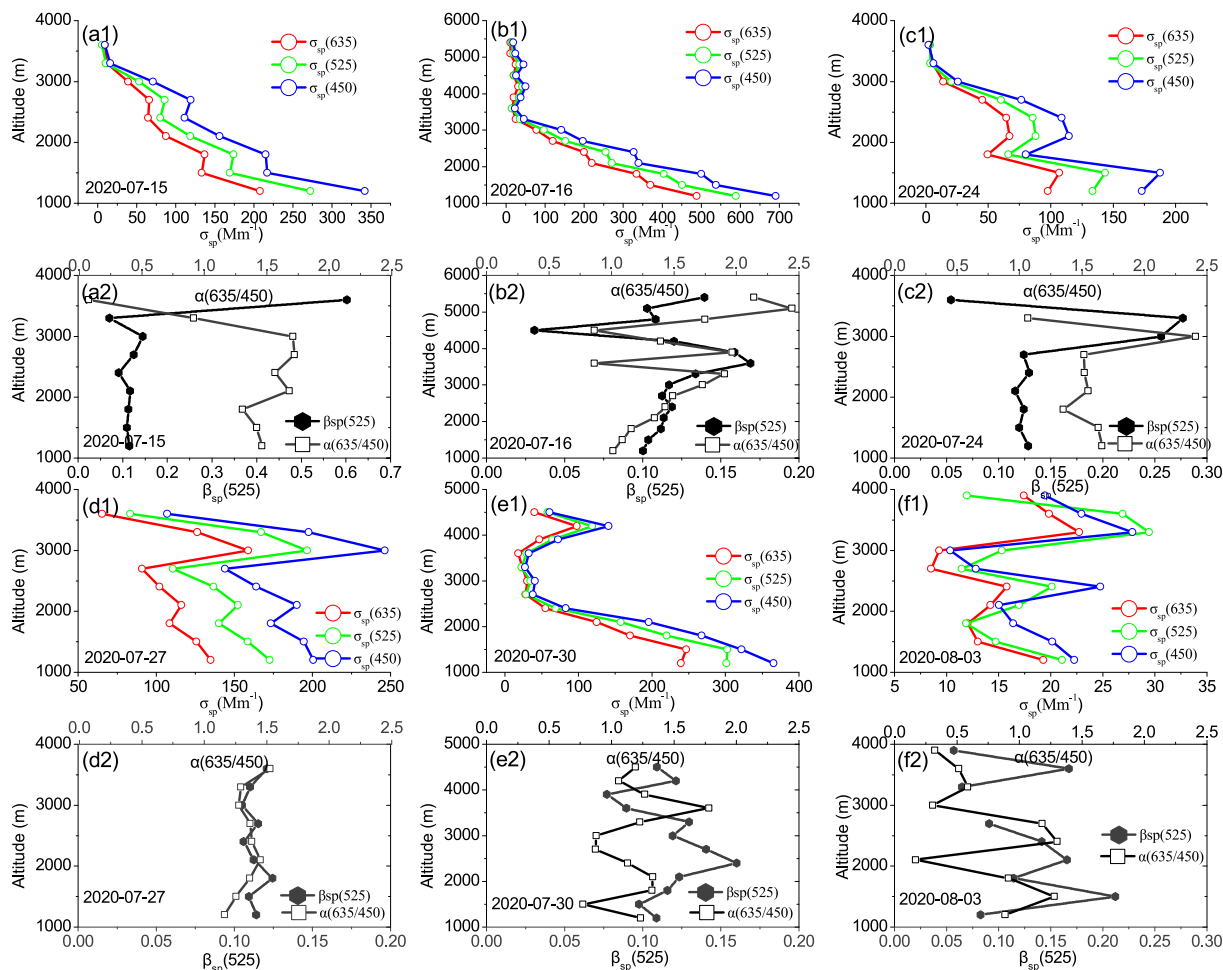| Altitude (m)	Mode I			Mode II			Mode II		
	N_a	D_g	Log σ	N_a	D_g	Log σ	N_a	D_g	Log σ
1000–2000	1500	0.18	0.17	130	0.35	0.2	0.6	2.2	0.1
2000–3000	1000	0.165	0.17	100	0.35	0.213	0.7	2	0.15
3000–4000	650	0.167	0.165	60	0.297	0.207	0.28	2.18	0.103
>4000	500	0.168	0.175	18	0.33	0.232	2	2.524	0.156

Fig. 5. Vertical profiles of mean aerosol scattering coefficient (σ_{sp}) at 450 nm (blue lines), 525 nm (green lines), and 635 nm (red lines), backscattering ratio ($\beta_{sp,525nm}$) (black lines with solid dots), and Ångström exponent ($\alpha_{635/450}$) (dark gray lines with hollow squares) on (a1, a2) 15 July, (b1, b2) 16 July, (c1, c2) 24 July, (d1, d2) 27 July, (e1, e2) 30 July, and (f1, f2) August 3, 2020. (For interpretation of the references to color in this figure legend, the reader is referred to the Web version of this article.)

geometric *MD* of the mode i, and$\sigma_{g,i}$ is the SD of mode i. The red, green, and blue solid lines in Fig. 4 show the lognormal fits of three modes to the mean aerosol particle spectrum, and the parameters that characterize the number size distributions of the three modes at different altitudes are listed in Table 2.

The shapes of aerosol spectrum are similar in the four height ranges. In general, there are three peaks at diameter around 0.165–0.18 μm (Mode I), 0.297–0.35 μm (Mode II), and 2.18–2.524 μm (Mode III). From the ground to 4000 m height, the total particle concentration decreased slightly, and the width of the particle spectral distribution narrows in Mode I, but broadens slightly in Mode III. According to the three modal lognormal distribution fitting, small particles (Mode I) dominated the particle number concentration, and the fitting parameters obtained here may be useful for the establishment and improvement of aerosol parameterization.

3.3. Vertical distributions of aerosol scattering properties

Light scattering by atmospheric aerosol particles affects Earth's energy balance, contributing to the negative radiative forcing of climate. The integrating nephelometer measures the aerosol scattering coefficient (σ_{sp}) at three wavelengths, i.e., 450, 525, and 635 nm. The 450-nm σ_{sp} provides information about fine and small particles, such as particles released by forest fires and automobile exhaust. The 525-nm and 635-nm σ_{sp}s are useful for characterizing smoke, fog, haze, and other

particles affecting atmospheric visibility and large particles, such as pollen and sea salt, respectively. Fig. 5 shows mean vertical profiles of σ_{sp} at the three wavelengths (Fig. 5a1, b1, c1, d1, e1, f1), and β_{sp} and α (Fig. 5a2, b2, c2, d2, e2, f2) measured during the six days of flights. Values of σ_{sp} at 450, 525, and 635 nm generally decreased with altitude except on 27 July (Fig. 5d1) and 3 August (Fig. 5f1). On the two hazy days, 16 July (Fig. 5b1) and 30 July (Fig. 5e1), values of σ_{sp} were higher. There were more pollutants in the atmosphere on 16 July, and N_a and σ_{sp} were much higher than on 3 August, the clear day. On 16 July (Fig. 5b1), maximum values of σ_{sp} (691.1, 588.6, and 488.6 Mm^{-1} at 450, 525, and 635 nm, respectively) appeared near the ground (1200 m ASL), decreasing with height gradually. On 3 August (Fig. 5f1), maximum values of σ_{sp} (27.8, 29.4, and 22.8 Mm^{-1} at 450, 525, and 635 nm, respectively) appeared at 3300 m ASL, with the vertical profile showing no clear trend. In combination with Fig. 3a, the maximum values of N_a and σ_{sp} appeared near the ground on 16 July. However, on 3 August, the maximum value of N_a appeared near the ground, and the maximum value of σ_{sp} appeared at a higher level. Overall, the magnitudes of N_a and σ_{sp} were ~6 and ~20 times greater in magnitude, respectively, on the hazy day (16 July) than on the clear day (3 August). Note that σ_{sp} reached peak values in the height range of ~3000–4000 m on 27 July (Fig. 5d1), 30 July (Fig. 5e1), and 3 August (Fig. 5f1), possibly related to local sources or the transportation of aerosol particles. This will be examined next.

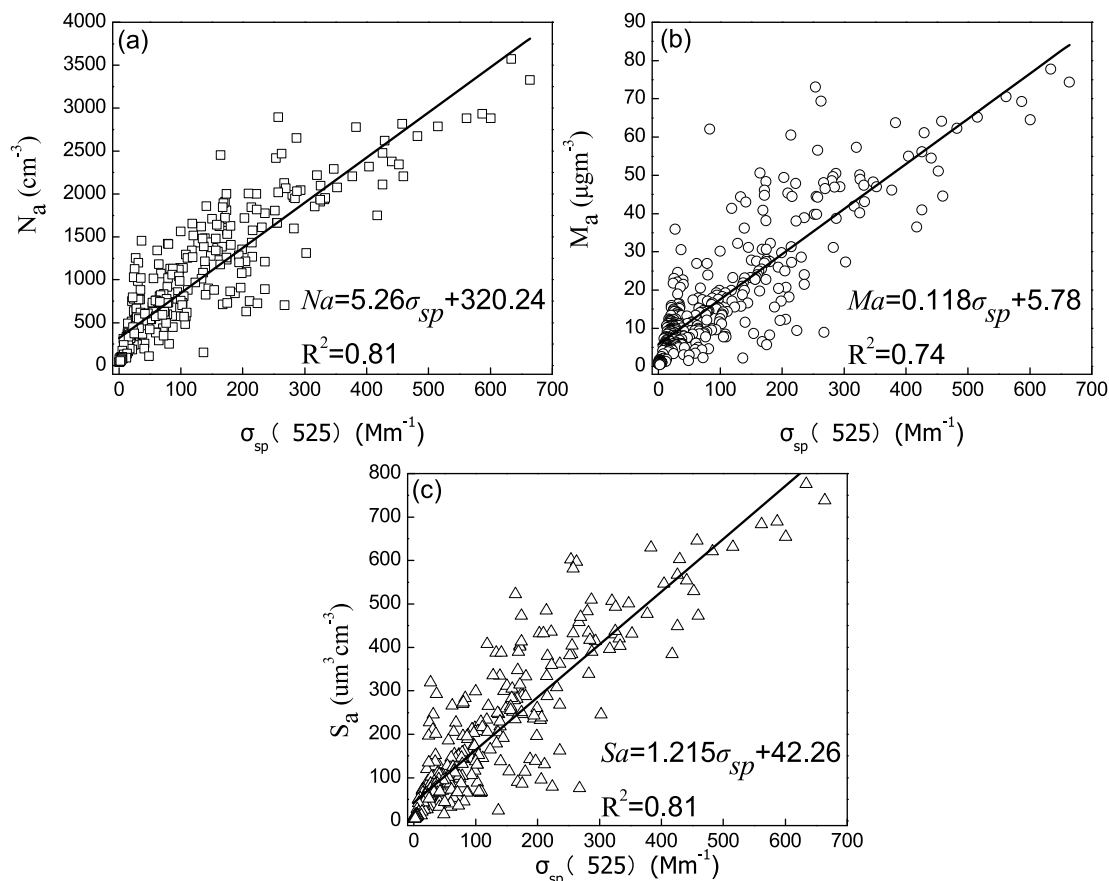β_{sp} can be used to evaluate aerosol-scattered radiation reaching the

Fig. 6. (a) Aerosol number concentration (N_a), (b) mass concentration (M_a), and (c) surface concentration (S_a) as a function of aerosol scattering coefficient (σ_{sp}) at 525 nm. The black lines are the best-fit lines from linear regression (equations and coefficients of determination are given in each panel).
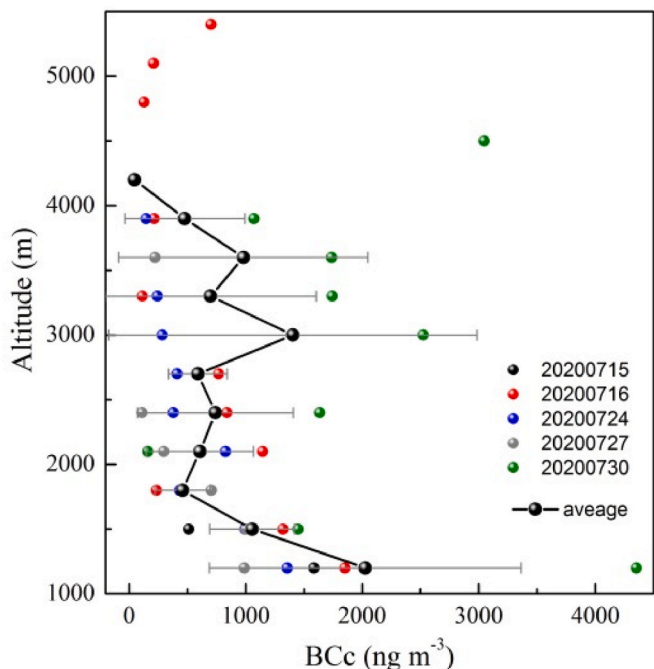

Fig. 7. Vertical distribution of the black carbon concentration (BC_c). Colored dots represent observations made on different days. Horizontal gray lines show the range of values (mean and standard deviation values) observed at each altitude level (above sea level).

ground, a quantity commonly required in radiative transfer models. The higher the ratio is, the greater the content of fine particles. In this study, because more attention is paid to the optical scattering effect of fog, haze, and other particles, only the vertical variation of β_{sp} at 525 nm is discussed (black lines in Fig. 5a2, b2, c2, d2, e2, and f2). The α is another important parameter that depends on the aerosol size distribution, increasing in magnitude as the particle size decreases. Aerosol type can be estimated using α. When scattering is dominated by coarse particles, α tends to be lower than 1 or even close to 0. This is a typical signature of desert-dust particles. When $\alpha > 1$, scattering is dominated by smaller particles (Seinfeld and Pandis, 1998). Fig. 5a2, b2, c2, d2, e2, and f2 show the vertical profiles of β_{sp} and α on the six days of flights. Values of β_{sp} (525 nm) were less than 0.15 in most cases and less than 0.3 in all cases. Values of α (635 nm/450 nm) mainly ranged from 1 to 2.5. This suggests that small aerosol particles were present during the field campaign, dominating the scattering.

In addition, the correlation between σ_{sp} and aerosol concentration was discussed. Fig. 6 shows scatterplots of N_a, M_a, and S_a as a function of σ_{sp} at 525 nm. Data are from all six flights. Linear fits were made to the data to determine the correlations between aerosol concentration and σ_{sp} without considering the influence of the chemical composition of aerosols. The coefficients of determination from linear regression are 0.81 (Figs. 6a), 0.74 (Fig. 6b), and 0.81 (Fig. 6c) according to the linear relations, i.e., $N_a = 5.26\sigma_{sp} + 320.24$, $M_a = 0.118\sigma_{sp} + 5.78$, and $S_a = 1.215\sigma_{sp} + 42.26$, respectively, suggesting the suitability of linear fits here.

3.4. Vertical distributions of BC_c, SSA and PAOD

Fig. 7 shows the vertical distribution of BC_c. Values of BC_c were
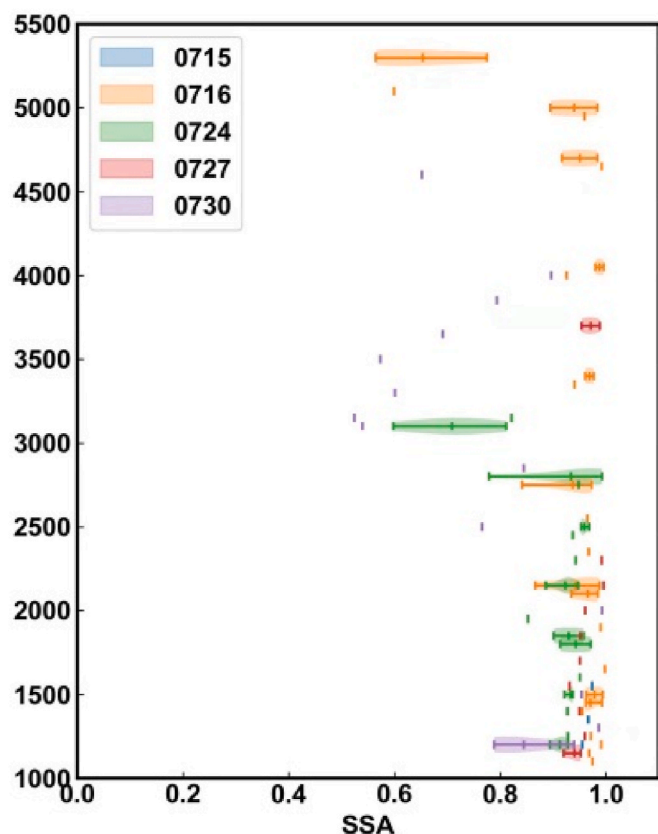
Fig. 8. The vertical distributions of the single-scattering albedo (SSA) on different days in July (colored areas). The middle points of each line segment are the mean values, and the end points represent minimum and maximum values, different colors represent the different observation days, and the shaded bars represents the frequency. (For interpretation of the references to color in this figure legend, the reader is referred to the Web version of this article.)

Fig. 9. Vertical distribution of partially-integrated AOD (PAOD) based on aircraft measurements.

two light fog days of 15 and 27 July. However, on the two hazy days (16 and 30 July), most SSA values were less than 0.85, with aerosols playing a warming role in the atmosphere.

In this study, we could only observe at a limited height range and perform extinction coefficient integration within the flight range because the flight height was limited. So the scattering coefficient was called partially-integrated aerosol optical depth (PAOD) in this paper. Fig. 9 shows the distribution of PAOD over different height ranges measured during the flights in July. Values of PAOD ranged from 0.3 to 0.9, with larger values between 1 and 2 km. Overall, aerosol loading in the layers 1–2 km, 2–3 km, and 3–4 km gradually decreased with height. Aerosols at 4–5 km reflect the long-distance transport of sand aerosols (seen on the hazy days of 16 and 30 July). Among the five flight days, aerosol loadings on 16 and 30 July were the highest, and the lowest on July 24, and moderate on 15 and 27 July.

4. Understanding the measurements and comparison with a previous air campaign

While the short-lived airborne campaign is unable to provide sufficient measurements to determine the "climatology" of aerosol loading and properties, the air-borne data do convey some valuable information to help understand it's changes.

4.1. Simulation of 48-h backward trajectories of air masses at different heights

According to the vertical profiles of N_a and ED_a (Fig. 3), aerosol particles at different heights may come from different sources. Forty-eight-hour backward trajectories of air masses were simulated using version 4.8 of the Hybrid of Single Particle Lagrangian Integrated Trajectory model to analyze the source of aerosol particles over XZ during the field campaign. The backward trajectory end point was the XZ station. Four heights (1000, 2000, 3000, and 4000 m ASL) were selected for the simulation. Fig. 10 shows the 48-h backward trajectories of air masses on the six days. On 24 July, particles in the 2000–3000-m layer mainly came from the Bohai Bay area, passing over Tianjin, Beijing, and Hebei before reaching the XZ station, and were mainly sea salt, automobile exhaust and other aerosol particles. Aerosols at the height of 4000 m mostly originate from the northwest of Shanxi province, mainly black carbon, sand and other absorbent aerosols. Combined with Section 3.4, it can be found that SSA values below 3000 m were greater than 0.8, and SSA values above 3000 m were lower than 0.6. On July 30, aerosols

largest near the ground, generally decreasing with altitude. Results below 2 km are similar to those reported in Beijing by Zhao et al. (2018). There was a large range of values of BC_c at the 3000-m level. A large value of BC occurred at 4500m height on July 30. In the flight on July 30, a strong updraft was observed and that could transport aerosols from the surface to higher positions. In addition, aerosols above 4 km were most dust particles transported over a long distance combined with the N_a vertical distribution, scattering characteristics and the air mass backward trajectory on July 30, 2020 (Section 4.1). In the long distance transport process, the particles might mix and aging with local black carbon aerosols, resulting in larger values of BC at the certain height.

The single-scattering albedo (SSA) plays an important role in studying the aerosol radiative effect (Anderson et al., 2003a) because this parameter reflects what proportion of the total extinction is due to scattering. When SSA is greater than 0.95, aerosols may have a cooling effect on the atmosphere (Haywood et al., 1997). When SSA is less than 0.85, aerosols may have a warming effect on both the atmosphere and the surface, even though the earth's surface may receive less sunlight (Haywood et al., 1998). Accurate measurements of SSA are thus important to evaluate the forcing effect of aerosols.

Fig. 8 shows the vertical variation of SSA at 525 nm over the XZ station. SSA values were generally greater than 0.9 below 2500 m, indicating that aerosol scattering dominated in this layer. Low values of SSA are mainly seen from 3000 to 4000 m, with a minimum value of 0.52, indicating that the absorbing effect of aerosols was dominant in this height range. Corresponding mean BC_c values in this layer were relatively high (Fig. 7), indicating the presence of a large proportion of absorbing aerosols in this layer. SSA values were greater than 0.9 on the
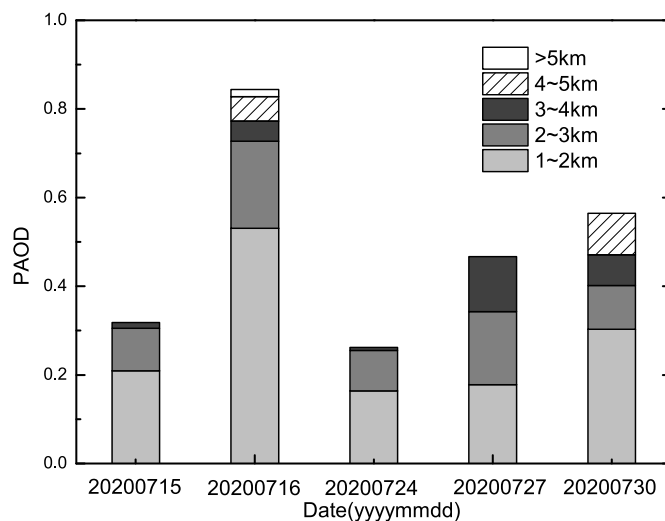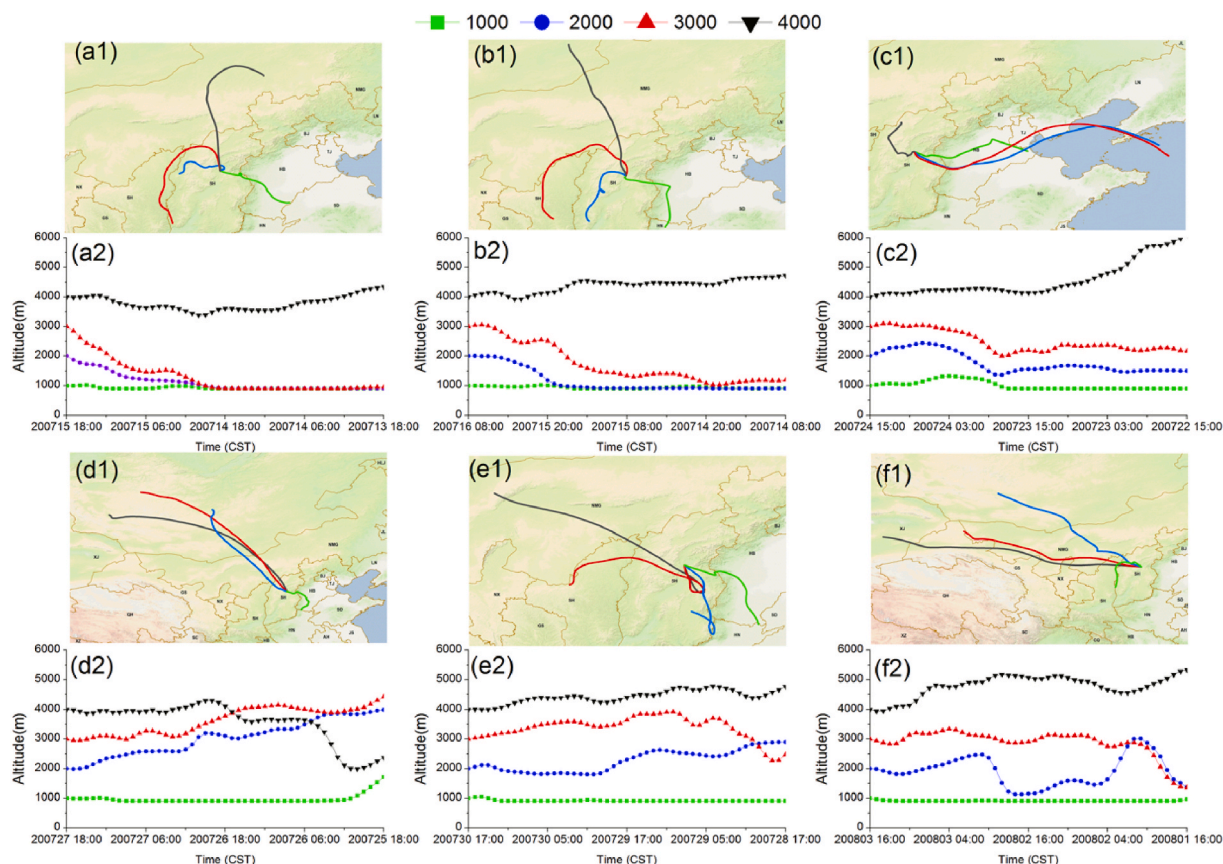
Fig. 10. Forty-eight-hour backward trajectories of air masses on (a1, a2) 15 July, (b1, b2) 16 July, (c1, c2) 24 July, (d1, d2) 27 July, (e1, e2) 30 July, and (f1, f2) August 3, 2020, with the Xinzhou station as the end point.

Table 3

Statistics describing aerosol microphysical and optical properties. S. D. stands for standard deviation.

Parameter	Maximum	Minimum	Mean ± S.D.	Median
N_a (cm^{-3})	3570.75	39.64	854.92 ± 713.75	597.20
V_a (μm^3 cm^{-3})	234.20	0.31	13.37 ± 19.08	7.68
M_a (μg m^{-3})	351.30	0.47	20.06 ± 28.63	11.53
S_a (μm^3 cm^{-3})	776.13	5.26	170.08 ± 168.08	95.41
ED_a (μm)	1.85	0.25	0.47 ± 0.17	0.41
BC_c (ng m^{-3})	10,198.82	15.03	1791.66 ± 2234.98	919.18
b_{abs} (880 nm) (Mm^{-1})	103.21	0.15	18.13 ± 22.62	9.30
σs_p635 nm) (Mm^{-1})	548.20	0.13	82.37 ± 98.62	41.09
σ_{sp} (525 nm) (Mm^{-1})	663.65	0.07	102.57 ± 120.42	53.30
σ_{sp} (450 nm) (Mm^{-1})	793.14	0.97	126.60 ± 145.41	65.65
σ_{bsp} (635 nm) (Mm^{-1})	57.21	0.01	10.25 ± 10.60	6.24
σ_{bsp} (525 nm) (Mm^{-1})	65.71	0.12	12.16 ± 12.74	7.36
σ_{bsp} (450 nm) (Mm^{-1})	86.09	0.04	15.09 ± 15.73	8.97
β_{sp} (525 nm)	23.78	0.01	0.23 ± 1.27	0.12
α(635 nm/450 nm)	6.03	0.07	1.47 ± 0.76	1.36
SSA (525 nm)	0.99	0.17	0.87 ± 0.17	0.94

above 4000 m were dust particles transported over a long distance, and the aerosols might mix and aging with local black carbon aerosols in the long distance transportation process, resulting in a higher value of black carbon and a lower value of SSA at 4500 m height. On 3 August, particles were mainly from northwest China, e.g., Xinjiang, northern Inner Mongolia, and Mongolia. The aerosols were dust particles of large size, low number concentration and weaker scattering than those of the other five observations. The vertical distributions of aerosol concentration and aerosol optical properties suggest that the majority of small particles at lower levels of the atmosphere from local or regional pollution emissions contributed the most to aerosol loading, especially on hazy days.

4.2. Comparison with a previous airborne campaign data

Table 3 summarizes statistics describing aerosol microphysical and optical properties observed during the field campaign. Mean values with standard deviations of N_a, V_a, M_a, and S_a were 854.92 ± 713.75 cm^{-3}, 13.37 ± 19.08 μm^3 cm^{-3}, 20.06 ± 28.63 μg/m^3, and 170.08 ± 168.08 μm^3 cm^{-3}, respectively. The ED_a of most aerosol particles was smaller than 1 μm during the field campaign, with a mean value of 0.47 ± 0.17 μm. Compared with values obtained at the same site and during the same season in 2013 (Li et al., 2015a), the magnitudes of N_a, V_a, M_a, and S_a declined significantly. For example, N_a decreased by 60% due to the decrease of small particles in the size range of 0.1–0.5 μm, and M_a decreased by 45% due to the decrease of larger particles in the size range of 0.8–3 μm. Values of BC_c ranged from 15.03 to 10,198.82 ng m^{-3}, with a mean value of 1791.66 ± 2234.98 ng m^{-3}, slightly greater than the observation in the summer of Beijing (Zhao et al., 2015, 2019), but far below than the observation during the winter of the North China and Central China (H. Zheng et al., 2018). The mean and standard deviation of σ_{sp} at 450, 525, and 635 nm were 126.60 ± 145.41 Mm^{-1}, 102.57 ± 120.42 Mm^{-1}, and 82.37 ± 98.62 Mm^{-1}, respectively, and the mean σ_{bsp} values at each of these wavelengths were 15.09 ± 15.73 Mm^{-1}, 12.16 ± 12.74 Mm^{-1}, and 10.25 ± 10.60 Mm^{-1}, respectively. Compared with the airborne measurements made in 2013 (Li et al., 2015b), the scattering coefficients increased in different degrees. The mean value of β_{sc} was 0.23 ± 1.27, and the value is larger than the observation in the North China Plain (Wang et al., 2018). The mean value of SSA was 0.87 ± 0.17, a slight increase from the mean value reported in 2013 (Li et al., 2015a), suggesting that the proportion of absorbing aerosols decreased.

The systematically lowered values of aerosol loading acquired from this experiment may echo the general reduction of air pollution across China (Wei et al., 2021), including the region of study. The spatial
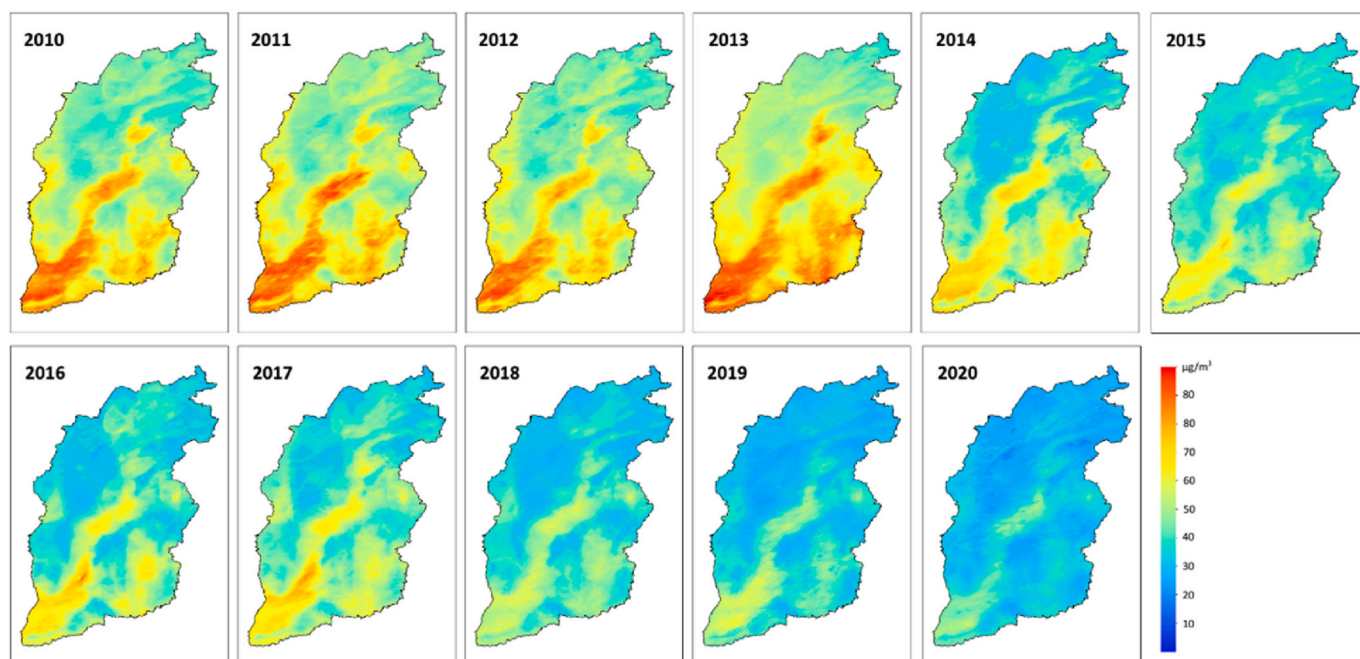
Fig. 11. Variations in Shanxi's PM$_{2.5}$ concentrations from 2010 to 2020.

distributions and variations of annual surface PM$_{2.5}$ in Shanxi Province from 2010 to 2020 were analyzed, using the high-resolution (1 km) and high-quality PM$_{2.5}$ dataset for China (i.e., ChinaHighPM$_{2.5}$). The ChinaHighPM$_{2.5}$ dataset was generated using satellite remote sensing data, surface observation data as inputs to machine learning models (Wei et al., 2020, 2021). Fig. 11 shows the variations of PM$_{2.5}$ concentration from 2010 to 2020 in Shanxi Province. Air pollution in Shanxi Province has changed significantly in recent years, which maintained at a relatively high level until 2013, and the average value was 59.54 ± 14.08 μg/m^3. In recent years, PM2.5 has decreased sharply due to the implemented National Clean Air Act (2013–2017) during which the mean PM$_{2.5}$ reduced to 44.99 ± 11.11 μg/m^3, followed by the Blue Sky Defense Plan (2018–2020) during which it further diminished to 33.47 ± 7.03 μg/m^3 (Zhang et al., 2019), the mean value of the PM$_{2.5}$ in 2020 decreased 49.1% compared to 2013, and these observation results are similar to those from the airborne observations. Such dramatic decline in ground-level particle concentration is bound to echo in the airborne measurements chiefly made inside the boundary layer.

It is worth noting that aircraft measurements are generally highly constrained by logistic conditions, weather, aerospace and funding supports. As such, it is infeasible to conduct large scale observations of long time series. We conducted four flights in our last airborne study (Li et al., 2015a), and six flights in this study of better instrumentation to help us gain more accurate measurements of aerosol properties in the Shanxi Province. As the two experiments were carried out in the same season and region, it allows us to make a comparative analysis between the two experiments, despite that the comparison results are somewhat circumstantial due to the small sample. On the other hand, drastic and persistent measures taken in combating air pollution across the region seem to have a noticeable effect on aerosol loading and properties, although caution needs to be exercised in interpreting the findings. The study just adds another piece of evidence of the large-scale declining trend of aerosol in northern China to the growing number of studies that were mostly from ground-based (Li et al., 2007, 2011, 2019a,b) or satellite observations (Geng et al., 2015; Wei et al., 2021). In this regard, our study is uniquely important for it provides the vertical profiles of aerosol loading and properties.

5. Conclusions

Aerosol parameters usually vary considerably in time and space and so are their climate effects. Among the various aerosol attributes, the vertical distributions of aerosol physical and optical properties are least known but they play critical roles in dictating its impact on atmospheric thermodynamics. Characterization of the vertical distribution of aerosol optical properties for studying aerosol's effects on local climate especially for modeling studies.

The vertical distributions of aerosol concentration and size distribution, as well as aerosol optical properties, were obtained through analyses of data collected during a summertime airborne field campaign in 2020 at the XZ station on the Loess Plateau in China. Statistics of the aerosol concentration, particle size, and aerosol optical properties were obtained and compared with results reported at the same station at the same time of the year in 2013 (Li et al., 2015a). Both α and β_{sp} values were relatively high, indicating that (1) scattering was dominated by fine particles and (2) a larger fraction of submicron particles dominated the total aerosol loading in the XZ region during the field campaign.

Analyzed were vertical profiles of N_a, M_a, S_a, and ED_a obtained during six flights. In general, large values of N_a appeared at lower altitudes. N_a decreased with height, showing two peaks, i.e., one at 1500 m and the other between 2000 and 2200 m. Fine particles with ED_a less than 0.8 μm comprised most of the total aerosol concentration during the aircraft measurement period. A multilognormal distribution function was used to fit the measured aerosol number size distributions. The fitting parameters obtained can provide a scientific reference for aerosol parameterization in numerical models.

Also analyzed were vertical profiles of σ_{sp} ($_{450,525,635\ nm}$), β_{sp} ($_{525\ nm}$), α ($_{635/450}$), and BC_c obtained during the six flights. In general, aerosol scattering properties and BCc in the lowest layer of the atmosphere contributed the most to the total aerosol radiative forcing, with values decreasing from the near surface to higher altitudes. Vertical profiles of β_{sp} and α were inversely correlated, with both parameters having relatively large values. This suggests that most aerosol particles observed were small, dominating scattering. A linear fit best expressed the relation between N_a and σ_{sc}.

Calculated and analyzed were SSA at 525 nm and PAOD. SSA was generally greater than 0.9 below 2500 m, with lower values of SSA

mainly appearing at higher levels. On light fog days, SSA was greater than 0.9, with aerosols playing a cooling role in the atmosphere. On hazy days, SSA in the lowest layer of the atmosphere was generally greater than 0.85.

Simulated using the Hybrid of Single Particle Lagrangian Integrated Trajectory model were 48-h backward trajectories of air masses for the field campaign period. The majority of particles in the lower atmosphere contributed the most to the total aerosol loading, leading to high values of aerosol concentration and radiative forcing. Most of these particles originated from local or regional pollution emissions.

CRediT authorship contribution statement

Zhaoxin Cai: Writing – original draft, conducted the bulk of the investigation and drafted the original manuscript. **Zhanqing Li:** proposed and guided the study. **Peiren Li:** designed and participated in aircraft campaign. **Junxia Li:** proposed and guided the study. **Hongping Sun:** designed and participated in aircraft campaign. **Yiman Yang:** Writing – review & editing, revised the manuscript. **Xin Gao:** Writing – review & editing, revised the manuscript. **Gang Ren:** operated and maintained the instruments used in the study. **Rongmin Ren:** operated and maintained the instruments used in the study. **Jing Wei:** Writing – review & editing, revised the manuscript.

Declaration of competing interest

The authors declare that they have no known competing financial interests or personal relationships that could have appeared to influence the work reported in this paper.

Acknowledgments

References

Anderson, T.L., Charlson, R.J., Schwartz, S.E., Knutti, R., Boucher, O., Rodhe, H., Heintzenberg, J., 2003a. Climate forcing by aerosols - a hazy picture. Science 300, 1103–1104. https://doi.org/10.1126/science.1084777.

Anderson, T.L., Masonis, S.J., Covert, D.S., Ahlquist, N.C., Howell, S.G., Clarke, A.D., McNaughton, C.S., 2003b. Variability of aerosol optical properties derived from in situ aircraft measurements during ACE-Asia. J. Geophys. Res. Atmos. 108 (D23) https://doi.org/10.1029/2002JD003247.

Bai, Y.B., Shi, G.Y., Tamura, K., Iwasaka, Y., 2000. Lidar observations of atmospheric aerosol optical properties over Lhasa. Chin. J. Atmos. Sci. 24, 559–567. https://doi.org/10.3878/j.issn.1006-9895.2000.04.12, 04.

Bodhaine, B.A., Ahlquist, N.C., Schnell, R.C., 1991. Three-wavelength nephelometer suitable for aircraft measurement of background aerosol scattering coefficient. Atmos. Environ. Part A. General Topics 25 (10), 2267–2276. https://doi.org/10.1016/0960-1686(91)90102-d.

Bohren, C.F., Huffman, D.R., 1998. Absorption and Scattering of Light by Small Particles. Wiley Interscience, New York, NY, p. 530.

Bond, T.C., Doherty, S.J., Fahey, D.W., Forster, P.M., Berntsen, T., DeAngelo, B.J., Flanner, M.G., Ghan, S., Kärcher, B., Koch, D., Kinne, S., Kondo, Y., Quinn, P.K., Sarofim, M.C., Schultz, M.G., Schulz, M., Venkataraman, C., Zhang, H., Zhang, S., Bellouin, N., Guttikunda, S.K., Hopke, P.K., Jacobson, M.Z., Kaiser, J.W., Klimont, Z., Lohmann, U., Schwarz, J.P., Shindell, D., Storelvmo, T., Warren, S.G., Zender, C.S., 2013. Bounding the role of black carbon in the climate system: a scientific assessment. J. Geophys. Res.: Atmos. 118 (11) https://doi.org/10.1002/jgrd.50171, 5380–5552.

Charlson, R.J., Schwartz, S.E., Hales, J.M., Cess, R.D., Coakley, J.A., Hansen, J.E., Hofmann, D.J., 1992. Climate forcing by anthropogenic aerosols. Science 255 (5043), 423–430. https://doi.org/10.1126/science.255.5043.423.

Chen, Y., Liu, Q., Geng, F., Zhang, H., Cai, C., Xu, T., Ma, X., Li, H., 2012. Vertical distribution of optical and micro-physical properties of ambient aerosols during dry haze periods in Shanghai. Atmos. Environ. 50, 50–59. https://doi.org/10.1016/j.atmosenv.2012.01.002.

Deshler, T., 2008. A review of global stratospheric aerosol: measurements, importance, life cycle, and local stratospheric aerosol. Atmos. Res. 90, 223–232. https://doi.org/10.1016/j.atmosres.2008.03.016.

Drinovec, L., Močnik, G., Zotter, P., Prévôt, A.S.H., Ruckstuhl, C., Coz, E., Rupakheti, M., Sciare, J., Müller, T., Wiedensohler, A., Hansen, A.D.A., 2015. The "dual-spot"

Aethalometer: an improved measurement of aerosol black carbon with real-time loading compensation. Atmos. Meas. Tech. 8, 1965–1979.

Ferrero, L., Castelli, M., Ferrini, B.S., Moscatelli, M., Perrone, M.G., Sangiorgi, G., Angelo, L.D.'., Rovelli, G., Moroni, B., Scardazza, F., Mocnik, G., Bolzacchini, E., Petitta, M., Cappelletti, D., 2014. Impact of black carbon aerosol over Italian basin valleys: high-resolution measurements along vertical profiles, radiative forcing and heating rate. Atmos. Chem. Phys. 14 (18), 9641–9664. https://doi.org/10.5194/acp-14-9641-2014.

Geng, F., Liu, Q., Chen, Y., Hua, Z., Xiaoqin, M., 2011. Preliminary study of vertical distribution of aerosols during dry haze periods around Shanghai based on CALIPSO. Procedia Earth Planet. Sci. 2, 217–222. https://doi.org/10.1016/j.proeps.2011.09.035.

Geng, G., Zhang, Q., Martin, R.V., van Donkelaar, A., Huo, H., Che, H., Lin, J., He, K., 2015. Estimating long-term PM2.5 concentrations in China using satellite-based aerosol optical depth and a chemical transport model. Rem. Sens. Environ. 166, 262–270. https://doi.org/10.1016/j.rse.2015.05.016.

Hagler, G.S.W., Yelverton, T.L.B., Vedantham, R., Hansen, A.D.A., Turner, J.R., 2011. Post-processing method to reduce noise while preserving high time resolution in aethalometer real-time black carbon data. Aerosol Air Qual Res 11, 539–546. https://doi.org/10.4209/aaqr.2011.05.0055.

Han, Z., Montague, D.C., Snider, J.R., 2003. Airborne measurements of aerosol extinction in the lower and middle troposphere over Wyoming, USA. Atmos. Environ. 37 (6), 789–802. https://doi.org/10.1016/s1352-2310(02)00952-4.

Hänel, G., 1998. Vertical profiles of the scattering coefficient of dry atmospheric particles over Europe normalized to air at standard temperature and pressure. Atmos. Environ. 32 (10), 1743–1755. https://doi.org/10.1016/s1352-2310(97)00460-3.

Hao, Y., Yin, Y., Kuang, X., Chen, J., Yuan, L., Xiao, H., Li, Z., Pu, M., Wang, J., Zhou, X., Chen, Y., Wu, Y., 2017. Aircraft measurements of the aerosol spatial distribution and relation with clouds over Eastern China. Aerosol Air Qual. Res. 17, 3230–3243. https://doi.org/10.4209/aaqr.2016.12.0576.

Haywood, J.M., Ramaswamy, V., 1998. Global sensitivity studies of the direct radiative forcing due to anthropogenic sulfate and black carbon aerosols. J. Geophys. Res.: Atmos. 103 (D6), 6043–6058. https://doi.org/10.1029/97jd03426.

Haywood, J.M., Shine, K.P., 1997. Multi-spectral calculations of the direct radiative forcing of tropospheric sulphate and soot aerosols using a column model. Q. J. R. Meteorol. Soc. 123 (543), 1907–1930. https://doi.org/10.1002/qj.49712354307.

Haywood, J.M., Roberts, D.L., Slingo, A., Edwards, J.M., Shine, K.P., 1997. General circulation model calculations of the direct radiative forcing by anthropogenic sulfate and fossil-fuel soot aerosol. J. Clim. 10 (7), 1562–1577. https://doi.org/10.1175/1520-0442(1997)010<1562:gcmcot>2.0.co;2.

Höpner, F., Bender, F.A.-M., Ekman, A.M.L., Praveen, P.S., Bosch, C., Ogren, J.A., Andersson, A., Gustafsson, Ö., Ramanathan, V., 2016. Vertical profiles of optical and microphysical particle properties above the northern Indian Ocean during CARDEX 2012. Atmos. Chem. Phys. 16 (2), 1045–1064. https://doi.org/10.5194/acp-16-1045-2016.

Horvath, H., 1995. Estimation of the average visibility in central Europe. Atmos. Environ. 29 (2), 241–246. https://doi.org/10.1016/1352-2310(94)00236-e.

Hu, K., Zhao, D., Liu, D., Ding, S., Tian, P., Yu, C., Zhou, W., Huang, M., Ding, D., 2020. Estimating radiative impacts of black carbon associated with mixing state in the lower atmosphere over the northern North China Plain. Chemosphere, 126455. https://doi.org/10.1016/j.chemosphere.2020.126455.

Jennings, S.G., Pinnick, R.G., Auvermann, H.J., 1978. Effects of particulate complex refractive index and particle size distribution variations on atmospheric extinction and absorption for visible through middle IR wavelengths. Appl. Opt. 17 (24), 3922–3929. https://doi.org/10.1364/ao.17.003922.

Johnson, B.T., Christopher, S., Haywood, J.M., Osborne, S.R., McFarlane, S., Hsu, C., Salustro, C., Kahn, R., 2009. Measurements of aerosol properties from aircraft, satellite and ground-based remote sensing: a case-study from the Dust and Biomass-burning Experiment (DABEX). Q. J. R. Meteorol. Soc. 135 (641), 922–934. https://doi.org/10.1002/qj.420.

Kang, L., Chen, S., Huang, J., Zhao, S., Ma, X., Yuan, T., Zhang, X., Xie, T., 2017. The spatial and temporal distributions of absorbing aerosols over East Asia. Rem. Sens. 9 (10), 1050. https://doi.org/10.3390/rs9101050.

Kaufman, Y.J., Hobbs, P.V., Kirchhoff, V.W.J.H., Artaxo, P., Remer, L.A., Holben, B.N., King, M.D., Ward, D.E., Prins, E.M., Longo, K.M., Mattos, L.F., Nobre, C.A., Spinhirne, J.D., Ji, Q., Thompson, A.M., Gleason, J.F., Christopher, S.A., Tsay, S.-C., 1998. Smoke, clouds, and radiation-Brazil (SCAR-B) experiment. J. Geophys. Res.: Atmos. 103 (D24), 31783–31808. https://doi.org/10.1029/98jd02281.

Ke, Z.J., Tang, J., 2007. An observation study of the scattering properties of aerosols over Shangdianzi, Beijing. Chin. J. Atmos. Sci. 31 (3), 553–559. https://doi.org/10.3878/j.issn.1006-9895.2007.03.19.

Li, Z., Chen, H., Cribb, M., Dickerson, R., Holben, B., Li, C., Lu, D., Luo, Y., Maring, H., Shi, G., Tsay, S.-C., Wang, P., Wang, Y., Xia, X., Zheng, Y., Yuan, T., Zhao, F., 2007. Preface to special section on East asian studies of tropospheric aerosols: an international regional experiment (EAST-AIRE). J. Geophys. Res. 112 (D22) https://doi.org/10.1029/2007jd008853.

Li, Z., Li, C., Chen, H., Tsay, S.-C., Holben, B., Huang, J., Li, B., Maring, H., Qian, Y., Shi, G., Xia, X., Yin, Y., Zheng, Y., Zhuang, G., 2011. East asian studies of tropospheric aerosols and their impact on regional climate (EAST-AIRC): an overview. J. Geophys. Res. 116 https://doi.org/10.1029/2010jd015257.

Li, J., Liu, X., Yuan, L., Yin, Y., Li, Z., Li, P., Ren, G., Jin, L., Li, R., Dong, Z., Li, Y., Yang, J., 2015a. Vertical distribution of aerosol optical properties based on aircraft measurements over the Loess Plateau in China. J. Environ. Sci. 34, 44–56. https://doi.org/10.1016/j.jes.2015.01.021.

Li, J., Yin, Y., Li, P., Li, Z., Li, R., Cribb, M., Dong, Z., Zhang, F., Li, J., Ren, G., Jin, L., Li, Y., 2015b. Aircraft measurements of the vertical distribution and activation

property of aerosol particles over the Loess Plateau in China. Atmos. Res. 155, 73–86. https://doi.org/10.1016/j.atmosres.2014.12.004.

Li, Z., Lau, W.K.-M., Ramanathan, V., Wu, G., Ding, Y., Manoj, M.G., Liu, J., Qian, Y., Li, J., Zhou, T., Fan, J., Rosenfeld, D., Ming, Y., Wang, Y., Huang, J., Wang, B., Xu, X., Lee, S.-S., Cribb, M., Zhang, F., Yang, X., Takemura, T., Wang, K., Xia, X., Yin, Y., Zhang, H., Guo, J., Zhai, P.M., Sugimoto, N., Babu, S.S., Brasseur, G.P., 2016. Aerosol and monsoon climate interactions over Asia. Rev. Geophys. 54 (4), 866–929. https://doi.org/10.1002/2015rg000500.

Li, J., Li, P., Yuan, L., Yin, Y., Wang, Z., Li, J., Li, Y., Ren, G., Cai, Z., 2017a. Physical and optical properties of atmospheric aerosols in summer at a suburban site in north China. Aerosol Air Qual. Res. 17, 1374–1388. https://doi.org/10.4209/aaqr.2016.12.0525.

Li, Z., Guo, J., Ding, A., Liao, H., Liu, J., Sun, Y., Wang, T., Xue, H., Zhang, H., Zhu, B., 2017b. Aerosols and boundary-layer interactions and impact on air quality. Natl. Sci. Rev. 4, 810–833. https://doi.org/10.1093/nsr/nwx117.

Li, J., Li, P., Ren, G., Yuan, L., Li, Y., Yang, J., 2019a. Aircraft measurements of aerosol distribution, warm cloud microphysical properties, and their relationship over the eastern Loess Plateau in China. Tellus B: Chem. Phys. Meteor. 71 (1), 1–18. https://doi.org/10.1080/16000889.2019.1663994.

Li, Z., Wang, Y., Guo, J., Cribb, M.C., Dong, X., Fan, J., Gong, D., Huang, J., Jiang, M., Jiang, Y., Lee, S.-S., Li, H., Li, J., Liu, J., Qian, Y., Rosenfeld, D., Shan, S., Sun, Y., Wang, H., Xin, J., Yan, X., Yang, X., Yang, X., Zhao, C., Zhang, F., Zheng, Y., 2019b. East asian study of tropospheric aerosols and their impact on regional clouds, precipitation, and climate (EAST-AIR CPC). J. Geophys. Res.: Atmos. https://doi.org/10.1029/2019jd030758.

Liu, P., Zhao, C., Liu, P., Deng, Z., Huang, M., Ma, X., Tie, X., 2009. Aircraft study of aerosol vertical distributions over Beijing and their optical properties. Tellus B 61 (5), 756–767. https://doi.org/10.1111/j.1600-0889.2009.00440.x.

Raes, F., Bates, T., McGovern, F., Van Liedekerke, M., 2000. The 2nd Aerosol Characterization Experiment (ACE-2): general overview and main results. Tellus B: Chem. Phys. Meteor. 52 (2), 111–125. https://doi.org/10.1034/j.1600-0889.2000.00124.x.

Ramanathan, V., Crutzen, P.J., Lelieveld, J., Mitra, A.P., Althausen, D., Anderson, J., Andreae, M.O., Cantrell, W., Cass, G.R., Chung, C.E., Clarke, A.D., Coakley, J.A., Collins, W.D., Conant, W.C., Dulac, F., Heintzenberg, J., Heymsfield, A.J., Holben, B., Howell, S., Hudson, J., Jayaraman, A., Kiehl, J.T., Krishnamurti, T.N., Lubin, D., McFarquhar, G., Novakov, T., Ogren, J.A., Podgorny, I.A., Prather, K., Priestley, K., Prospero, J.M., Quinn, P.K., Rajeev, K., Rasch, P., Rupert, S., Sadourny, R., Satheesh, S.K., Shaw, G.E., Sheridan, P., Valero, F.P.J., 2001. Indian Ocean Experiment: an integrated analysis of the climate forcing and effects of the great Indo-Asian haze. J. Geophys. Res.: Atmos. 106 (D22), 28371–28398. https://doi.org/10.1029/2001jd900133.

Raut, J.C., Chazette, P., 2008. Vertical profiles of urban aerosol complex refractive index in the frame of ESQUIF airborne measurements. Atmos. Chem. Phys. 8 (4), 901–919. https://doi.org/10.5194/acp-8-901-2008.

Russell, P.B., Livingston, J.M., Hignett, P., Kinne, S., Wong, J., Chien, A., Bergstrom, R., Durkee, P., Hobbs, P.V., 1999. Aerosol-induced radiative flux changes off the United States mid-Atlantic coast: comparison of values calculated from sunphotometer and in situ data with those measured by airborne pyranometer. J. Geophys. Res.: Atmos. 104 (D2), 2289–2307. https://doi.org/10.1029/1998jd200025.

Seinfeld, J.H., Pandis, S.N., 1998. Atmospheric Chemistry and Physics: From Air Pollution to Climate Change. John Wiley and Sons, New York.

Shen, J., Cao, N., 2020. Comprehensive Observation and Analysis of Aerosol Optical Properties and Vertical Distribution in Nanjing, China. Atmospheric Environment, 117767. https://doi.org/10.1016/j.atmosenv.2020.117767.

Song, Z., He, X., Bai, Y., Wang, D., Hao, Z., Gong, F., Zhu, Q., 2020. Changes and predictions of vertical distributions of global light-absorbing aerosols based on CALIPSO observation. Rem. Sens. 12 (18), 3014. https://doi.org/10.3390/rs12183014.

Stettler, M., von Hoyningen-Huene, W., 1996. On the relation between haze layer and air mass function at an urban location - case studies. Atmos. Res. 40 (1), 1–18. https://doi.org/10.1016/0169-8095(95)00029-1.

Sun, Y., Wang, Y., Zhang, C., 2010. Vertical observations and analysis of PM$_{2.5}$, O$_3$, and NOx at Beijing and Tianjin from towers during summer and autumn 2006. Adv. Atmos. Sci. 27 (1), 123–136. https://doi.org/10.1007/s00376-009-8154-z.

Sun, X., Yin, Y., Sun, Y., Sun, Y., Liu, W., Han, Y., 2013. Seasonal and vertical variations in aerosol distribution over Shijiazhuang, China. Atmos. Environ. 81, 245–252. https://doi.org/10.1016/j.atmosenv.2013.08.009.

Sun, H., Li, P., Sheng, D., Yang, J., 2016. Aerosol vertical distribution characteristics and optical properties by aircraft measurements on Loess plateau. China Environ. Sci. 36 (8), 2311–2322. https://doi.org/10.3969/j.issn.1000-6923.2016.08.010.

Virkkula, A., Makela, T., Hillamo, R., Yli-Tuomi, T., Hirsikko, A., Hameri, K., Koponen, I. K., 2007. A simple procedure for correcting loading effects of aethalometer data. J. Air Waste Manag. Assoc. 57, 1214–1222. https://doi.org/10.3155/1047-3289.57.10.1214.

Wang, F., Li, Z., Ren, X., Jiang, Q., He, H., Dickerson, R., Dong, X., Lv, F., 2018. Vertical distributions of aerosol optical properties during the spring 2016 ARIAs airborne campaign in the North China Plain. Atmos. Chem. Phys. 18 (12), 8995–9010. https://doi.org/10.5194/acp-18-8995-2018.

Wang, Q., Wang, L., Li, X., Xin, J., Liu, Z., Sun, Y., Liu, J., Zhang, Y., Du, W., Jin, X., Zhang, T., Liu, S., Liu, Q., Chen, J., Cheng, M., Wang, Y., 2020. Emission characteristics of size distribution, chemical composition and light absorption of particles from field-scale crop residue burning in Northeast China. Sci. Total Environ. 710. https://doi.org/10.1016/j.scitotenv.2019.136304.

Wei, J., Li, Z., Cribb, M., Huang, W., Xue, W., Sun, L., Guo, J., Peng, Y., Li, J., Lyapustin, A., Liu, L., Wu, H., Song, Y., 2020. Improved 1kmresolution PM2 .5estimates across China using enhanced space -timeextremely randomized trees. Atmos. Chem. Phys. 20, 3273–3289. https://doi.org/10.5194/acp-20-3273-2020.

Wei, J., Li, Z., Lyapustin, A., Sun, L., Peng, Y., Xue, W., Su, T., Cribb, M., 2021. Reconstructing 1-km-resolution high-quality PM2.5 data records from 2000 to 2018 in China: spatiotemporal variations and policy implications. Rem. Sens. Environ. 252, 112136 https://doi.org/10.1016/j.rse.2020.112136.

Welton, E.J., Voss, K.J., Quinn, P.K., Flatau, P.J., Markowicz, K., Campbell, J.R., Spinhirne, J.D., Gordon, H.R., Johnson3, James E., 2002. Measurements of aerosol vertical profiles and optical properties during INDOEX 1999 using micropulse lidars. J. Geophys. Res. Atmos. 107 (D19) https://doi.org/10.1029/2000JD000038.

Wu, D., Mao, J., Deng, X., Tie, X., Zhang, Y., Zeng, L., Li, F., Tan, H., Bi, X., Huang, X., Chen, J., Deng, T., 2009. Black carbon aerosols and their radiative properties in the Pearl River Delta region. Sci. China Earth Sci. 52 (8), 1152–1163. https://doi.org/10.1007/s11430-009-0115-y.

Wu, Y., Zhang, R., Pu, Y., Zhang, L., Ho, K.F., Fu, C., 2012. Aerosol optical properties observed at a semi-arid rural site in northeastern China. Aerosol Air Qual. Res. 12, 503–514. https://doi.org/10.4209/aaqr.2011.11.0202.

Yamaji, K., Li, J., Uno, I., Kanaya, Y., Irie, H., Takigawa, M., Komazaki, Y., Pochanart, P., Liu, Y., Tanimoto, H., Ohara, T., Yan, X., Wang, Z., Akimoto, H., 2010. Impact of open crop residual burning on air quality over Central Eastern China during the Mount Tai Experiment 2006 (MTX2006). Atmos. Chem. Phys. 10 (15), 7353–7368. https://doi.org/10.5194/acp-10-7353-2010.

Yan, H., 2007. Aerosol scattering properties in northern China. Atmos. Environ. 41 (32), 6916–6922. https://doi.org/10.1016/j.atmosenv.2007.04.052.

Yan, P., Tang, J., Huang, J., Mao, J.T., Zhou, X.J., Liu, Q., Wang, Z.F., Zhou, H.G., 2008. The measurement of aerosol optical properties at a rural site in Northern China. Atmos. Chem. Phys. 8 (8), 2229–2242. https://doi.org/10.5194/acp-8-2229-2008.

Yang, J., Li, J., Li, P., Sun, G., Cai, Z., Yang, X., Cui, C., Dong, X., Xi, B., Wan, R., Wang, B., Zhao, Z., 2020. Spatial distribution and impacts of aerosols on clouds under Meiyu frontal weather background over central China based on aircraft observations. J. Geophys. Res. Atmos. 125, e2019JD031915 https://doi.org/10.1029/2019JD031915.

Yuan, L., Yin, Y., Xiao, H., Yu, X., Hao, J., Chen, K., Liu, C., 2016. A closure study of aerosol optical properties at a regional background mountainous site in Eastern China. Sci. Total Environ. 550, 950–960. https://doi.org/10.1016/j.scitotenv.2016.01.205.

Yuan, L., Yin, Y., Xiao, H., Hao, J., Chen, K., Yu, X., Zhang, X., 2019. Aerosol optical properties and the mixing state of black carbon at a background mountainous site in Eastern China. J. Environ. Sci. 83, 21–38. https://doi.org/10.1016/j.jes.2019.03.013.

Zeng, Y., Cao, Y., Qiao, X., Seyler, B.C., Tang, Y., 2019. Air pollution reduction in China: recent success but great challenge for the future. Sci. Total Environ. https://doi.org/10.1016/j.scitotenv.2019.01.262.

Zhang, D., Aunan, K., Martin Seip, H., Larssen, T., Vennemo, H., Larssen, S., Feng, L., Wu, C., Xie, R., 2012. Air pollution reduction during China's 11th Five-Year Plan period—local implementation and achievements in Shanxi province. Environ. Develop. 4, 36–53. https://doi.org/10.1016/j.envdev.2012.09.002.

Zhang, Q., Zheng, Y., Tong, D., Shao, M., Wang, S., Zhang, Y., Xu, X., Wang, J., He, H., Liu, W., Ding, Y., Lei, Y., Li, J., Wang, Z., Zhang, X., Wang, Y., Cheng, J., Liu, Y., Shi, Q., Yan, L., Geng, G., Hong, C., Li, M., Liu, F., Zheng, B., Cao, J., Ding, A., Gao, J., Fu, Q., Huo, J., Liu, B., Liu, Z., Yang, F., He, K., Hao, J., 2019. Drivers of Improved PM2.5 Air Quality in China from 2013 to 2017. Proceedings of the National Academy of Sciences, 201907956. https://doi.org/10.1073/pnas.1907956116.

Zhao, X.J., Zhang, X.L., Pu, W.W., Meng, W., Xu, X., 2011. Scattering properties of the atmospheric aerosol in Beijing, China. Atmos. Res. 101 (3), 799–808. https://doi.org/10.1016/j.atmosres.2011.05.010.

Zhao, D., Tie, X., Gao, Y., Zhang, Q., Tian, H., Bi, K., Jin, Y., Chen, P., 2015. In-situ aircraft measurements of the vertical distribution of black carbon in the lower troposphere of Beijing, China, in the spring and summer time. Atmosphere 6 (5), 713–731. https://doi.org/10.3390/atmos6050713.

Zhao, D., Huang, M., Liu, D., Ding, D., Tian, P., Liu, Q., Zhou, W., Sheng, J., Wang, F., Bi, K., Yang, Y., Li, X., Hu, Y., Guo, X., Gao, Y., He, H., Chen, Y., Kong, S., Huang, J., 2018. Aircraft measurements of black carbon in the boundary layer over the North China Plain. Atmos. Chem. Phys. Discuss. 1–25. https://doi.org/10.5194/acp-2017-1118.

Zhao, D., Huang, M., Tian, P., He, H., Lowe, D., Zhou, W., Sheng, J., Wang, F., Bi, K., Kong, S., Yang, Y., Liu, Q., Liu, D., Ding, D., 2019. Vertical characteristics of black carbon physical properties over Beijing region in warm and cold seasons. Atmos. Environ. 213, 296–310. https://doi.org/10.1016/j.atmosenv.2019.06.007.

Zheng, B., Tong, D., Li, M., Liu, F., Hong, C., Geng, G., Li, H., Li, X., Peng, L., Qi, J., Yan, L., Zhang, Y., Zhao, H., Zheng, Y., He, K., Zhang, Q., 2018a. Trends in China's anthropogenic emissions since 2010 as the consequence of clean air actions. Atmos. Chem. Phys. Discuss. 1–27. https://doi.org/10.5194/acp-2018-374.

Zheng, H., Kong, S., Wu, F., Cheng, Y., Niu, Z., Zheng, S., Yang, G., Yao, L., Yan, Q., Wu, J., Zheng, M., Chen, N., Xu, K., Yan, Y., Liu, D., Zhao, D., Zhao, T., Bai, Y., Li, S., Qi, S., 2018b. Intra-regional transport of black carbon between the south edge of North China Plain and Central China during winter haze episodes. Atmos. Chem. Phys. Discuss. 1–35. https://doi.org/10.5194/acp-2018-992.

Zhuang, B.L., Wang, T., Liu, J., Ma, Y., Yin, C.Q., Li, S., Xie, M., Han, Y., Zhu, J.L., Yang, X.Q., Fu, C.B., 2015. Absorption coefficient of urban aerosol in Nanjing, west Yangtze River Delta, China. Atmos. Chem. Phys. 15 (23), 13633–13646. https://doi.org/10.5194/acp-15-13633-2015.